Defect chemistry and transport properties of $Ba_xCe_{0.85}M_{0.15}O_{3-\delta}$

J. Wu,[a] L.P. Li,[b] W.T.P. Espinosa,[c] and S.M. Haile
Material Science, California Institute of Technology, Pasadena, California 91125

(Received 17 November 2003; accepted 30 April 2004)

The site-incorporation mechanism of M^{3+} dopants into $A^{2+}B^{4+}O_3$ perovskites controls the overall defect chemistry and thus their transport properties. For charge-balance reasons, incorporation onto the A^{2+}-site would require the creation of negatively charged point defects (such as cation vacancies), whereas incorporation onto the B^{4+}-site is accompanied by the generation of positively charged defects, typically oxygen vacancies. Oxygen-vacancy content, in turn, is relevant to proton-conducting oxides in which protons are introduced via the dissolution of hydroxyl ions at vacant oxygen sites. We propose here, on the basis of x-ray powder diffraction studies, electron microscopy, chemical analysis, thermal gravimetric analysis, and alternating current impedance spectroscopy, that nominally B-site doped barium cerate can exhibit dopant partitioning as a consequence of barium evaporation at elevated temperatures. Such partitioning and the presence of significant dopant concentrations on the A-site negatively impact proton conductivity. Specific materials examined are $Ba_xCe_{0.85}M_{0.15}O_{3-\delta}$ ($x = 0.85 - 1.20$; M = Nd, Gd, Yb). The compositional limits for the maximum A-site incorporation are experimentally determined to be: $(Ba_{0.919}Nd_{0.081})(Ce_{0.919}Nd_{0.081})O_3$, $(Ba_{0.974}Gd_{0.026})(Ce_{0.872}Gd_{0.128})O_{2.875}$, and $Ba(Ce_{0.85}Yb_{0.15})O_{2.925}$. As a consequence of the greater ability of larger cations to exist on the Ba site, the H_2O adsorption and proton conductivities of large-cation doped barium cerates are lower than those of small-cation doped analogs.

I. INTRODUCTION

Charge transport in doped transition metal perovskites (e.g., $LaMnO_3$ and derivatives) by both oxygen ions and/or electrons has been widely studied and such materials find applications in a broad range of electrochemical and other devices.[1,2] More recently, high proton conductivity has been established in doped $A^{2+}B^{4+}O_3$ perovskites such as $BaCeO_3$, $SrCeO_3$, and $SrZrO_3$.[3–6] The particularly high conductivity of rare-earth (or yttrium) doped $BaCeO_3$ has led to extensive studies of its applicability as an electrolyte for reduced-temperature solid-oxide fuel cells and for hydrogen sensors.[7,8]

Proton incorporation in $BaCeO_3$ has been generally recognized to occur by two steps:

$$2Ce_{Ce}^{x} + O_o^{x} + M_2O_3 \rightarrow 2M'_{Ce} + V^{\bullet\bullet}_o + 2CeO_2 \quad , \tag{1}$$

$$H_2O\ (gas) + V^{\bullet\bullet}_o + O_o^{x} \rightarrow 2OH^{\bullet}_o \quad , \tag{2}$$

where M is the trivalent dopant species. In the first step, introduction of M^{3+} ions on the Ce^{4+} site creates oxygen vacancies within the perovskite structure. In the second, the exposure of the doped material to humid atmosphere leads to the incorporation of hydroxyl groups onto formerly vacant oxygen sites, and of protons at other oxygen sites. To facilitate reaction (1) and encourage dopant incorporation onto the tetravalent site, samples are prepared with general composition $BaCe_{1-z}M_zO_{3-\delta}$.

In contrast to the simple dopant incorporation mechanism implied in Eq. (1), in which the entirety of the dopant species resides on the B-site of the perovskite oxide, it has been shown (through a careful phase diagram study) that Nd in particular can be partitioned over

[a]Address all correspondence to this author.
e-mail: jwu@caltech.edu
[b]Present address: Department of Physics and Astronomy, Brigham Young University, Provo, Utah 84602.
[c]Present address: Boeing Rocketdyne Propulsion and Power, 6633 Canoga Avenue FB19, Canoga Park, California 91309.
DOI: 10.1557/JMR.2004.0302

both A- and B-sites of barium cerate ceramics in which the total Ba/(Ce+Nd) molar ratio is less than one.[9] Such an observation is perhaps not unexpected given the relative ionic radii of the three species involved, with Nd being intermediate in size between Ce and Ba. Experimental evidence for the existence of similarly "amphoteric" dopants in $BaTiO_3$ has also been recently reported.[10] In a study more directly focused on proton conducting perovskites, it was proposed that even in samples with nominal stoichiometry Ba/(Ce+M) = 1 partial incorporation of trivalent dopants onto the Ba-site of barium cerate can occur as a consequence of BaO loss at high temperatures.[11] Such incorporation of the dopant onto the "wrong" site, in turn, can be anticipated to have a profound effect on proton conductivity by lowering the concentration of oxygen vacancies to a value less than $[V_o^{\bullet\bullet}] = \frac{1}{2}[M]$, which would be predicted by Eq. (1), and thereby reducing water uptake [Eq. (2)] from its ideal value.

The role of barium evaporation from barium cerate in establishing the perovskite defect chemistry and proton conductivity has not been explored, although barium loss is occasionally discussed by practitioners in the field. In the absence of dopants that can reside on the Ba-site, barium deficiency can, in principle, result in either the formation of a single-phase perovskite with a high concentration of barium vacancies on the Ba-site, or the precipitation of the CeO_2 fluorite phase. Although vacancies are known to occur on the A-site of $A^{2+}B^{4+}O_3$ perovskites (such as barium titanate),[12,13] precipitation of ceria has been observed in the case of barium-deficient, undoped barium cerate.[11,14] In the presence of dopants, in contrast, ceria precipitation is much less extensive. Thus, dopant partitioning has been identified as the mechanism by which the perovskite phase is stabilized in doped, barium-deficient compositions. Recent computational studies also support a defect chemical model for M^{3+} doped $A^{2+}B^{4+}O_3$ perovskites in which dopants distribute over the two cation sites; and that the effect, perhaps predictably, is greatest for large dopant ions.[15,16] In the present work, we extend the experimental investigation of barium cerate to three species, Yb, Gd, and Nd, and we use a broad range of characterization tools to comprehensively study the question of site-incorporation selectivity, its relationship to compositional nonstoichiometry, and its impact on proton conductivity.

II. EXPERIMENTAL

Materials examined in this work were synthesized by both solid-state reaction (SSR) and chemical-solution methods (MP). The latter were prepared to establish whether chemical homogeneity had a significant impact on the defect chemistry of the materials. The trends were found to be similar; and given the relative ease of solid-state synthesis, the majority of the experiments were carried out on $Ba_xCe_{0.85}M_{0.15}O_3$ (M = Nd, Gd, Yb; x = 0.85–1.20) SSR samples, prepared as follows. Starting materials (from Alfa Aesar) of $BaCO_3$ (99.95%), CeO_2 (99.9%), M_2O_3 (99.9%) (M = Nd, Gd, Yb) were ball-milled in acetone for 48 h and subsequently calcined in air at 1300 °C for 6 h. The calcined samples were lightly ground and a second calcination step was carried out at 1300 °C for another 6 h to ensure that a single perovskite phase was formed. Green pellets (9 mm in diameter) were obtained by dry pressing at 150 MPa and isostatic pressing at 270 MPa. High density pellets (≥94% of theoretical) were obtained by sintering in air at 1550 °C for 4 h. Density was determined by simple measurements of pellet mass and dimensions after polishing the surfaces.

Chemical-solution synthesis of $Ba_xCe_{0.85}M_{0.15}O_3$ (M = Nd, Gd, Yb; x = 0.95–1.05) followed the modified Pechini (MP) process of Aragwal and Liu.[17] The precursors $Ba(NO_3)_2$, $Ce(NO_3)_3{\cdot}6H_2O$, $Nd(NO_3)_3{\cdot}6H_2O$, $Yb(NO_3)_3{\cdot}4.44H_2O$, and $Gd(NO_3)_3{\cdot}5.45H_2O$ (the water content in the Yb and Gd nitrates was determined by thermogravimetric analysis) were dissolved in water along with ethylenediaminetetraacetic acid (EDTA) and ethylene glycol (EG), which served as polymerization/complexation agents. The molar ratios EDTA/ΣMetal and EDTA/EG were fixed at 2 and 1/3, respectively. Evaporation of water and polymerization of the ethylene glycol occurred upon mild heating, and the resulting char was calcined at 1300 °C for 10 h. High-density pellets (≥94% of theoretical) were obtained under the same sintering conditions used for the solid-state reaction samples. A third set of sintered pellets, all of composition $BaCe_{0.85}Gd_{0.15}O_{3-\delta}$, were obtained by pressing the chemically synthesized powders using poly(vinyl alcohol) as a binder and then sintering for 4 h at 1500 °C, 1550 °C, 1600 °C, or 1650 °C. These samples were prepared to explicitly examine the influence of high-temperature processing on defect chemistry.

Powder x-ray diffraction measurements were collected in reflection mode at room temperature and under ambient conditions with a Siemens D-500 powder diffractometer using CuKα radiation. Nickel powder (99.99%) served as an internal standard for peak-position determination. Data were collected from both calcined and sintered SSR samples; calcined samples after the second heat treatment, and sintered samples after polishing away surface regions and regrinding the pellets. In the case of MP samples, diffraction data were obtained only after calcination, with the exception of the $BaCe_{0.85}Gd_{0.15}O_{3-\delta}$ sintered at different temperatures. For all samples, measurements were performed soon after synthesis to minimize any influence of water uptake. The lattice parameters were refined on the basis of 12 peak positions using

the Rietica Rietveld program.[18] Use of a Rietveld program ensured that peak indexing was accurate. Attempts to carry out complete analysis of structural parameters (in particular, site occupancies) were unsuccessful because of the similarity of the scattering lengths of the cations involved and the limited range (20–90° 2Θ) over which data could be collected. The structure of undoped $BaCeO_3$ as reported by Knight and Bonanos[19] (orthorhombic Pbnm with a = 6.236Å, b = 6.216 Å, c = 8.777 Å) served as the starting point for the refinements.

Chemical analysis was performed by both electron microprobe methods (JEOL JXA-733 EMP, 15 kv, 25 nA) and energy-dispersive spectrometry (EDS), the latter in conjunction with scanning electron microscopy (JEOL 5200, SEM). Electron microprobe analysis (employing wavelength dispersive spectroscopy) was used primarily for quantitative measurements of the average chemical compositions of sintered pellets. In addition, the surface-to-interior composition gradient of a sintered pellet of nominally stoichiometric $BaCe_{0.85}Gd_{0.15}O_{3-\delta}$ was measured by electron microprobe analysis. The EDS method, with its high spatial resolution, was used to determine compositional differences between bulk and grain boundary regions of selected sintered pellets. All samples for these analyses were mounted in an epoxy resin, cut, polished, and coated with a conductive layer of carbon. Prior to carbon coating, samples for EDS analysis were etched with concentrated HF for several minutes to reveal grain boundaries. Characteristic x-ray emission intensities of the specific elements, as measured in the microprobe, were converted to chemical weight percents and molar ratios with the program CITZAF.[20] The Lβ1 line of Ce was collected to avoid interference with the Lβ emission of Ba. The compounds $CePO_4$, $GdPO_4$, $NdPO_4$, $YbPO_4$, and $BaTiSi_3O_9$ served as standards for quantification of the x-ray intensities. Neither standards nor an adequate means of deconvoluting overlapping peaks were used for the EDS analysis and only the ratios of the characteristic peak intensities were recorded for those samples.

Thermal gravimetric analysis (TGA) of H_2O-saturated sintered pellets (saturated at 500 °C for 20 h, in a flowing water-saturated argon atmosphere) was performed in flowing dry Ar at a heating rate of 20 °C/min over the temperature range from 100 to 1000 °C, to assess H_2O-incorporation ability. The data were collected with a Netzsch STA 449. The exhaust gases released during the heating process were examined by mass spectroscopy (Balzers, AMU200).

The transport properties of sintered pellets were measured by ac impedance spectroscopy over a frequency range from 20 Hz to 1 MHz using an HP 4284A LCR (inductance-capacitance-resistance) meter. Platinum electrodes were sputter-coated onto the opposing sides of polished pellets. Samples were equilibrated in water-saturated Ar at 400 °C for 2 h. The data were collected upon cooling at a rate of 0.5 °C/min. The amplitude of the voltage was 1 V. Measurement wires were electrically shielded so as to reduce noise in the data, and zero and open circuit corrections were applied to eliminate the effects of stray capacitances and/or inductances. Impedance data were fit to an equivalent circuit model using the least-squares refinement program EQUIVCRT,[21] enabling direct measurement of the equivalent bulk direct current conductivity, without influence of grain boundary contributions to resistance.

III. RESULTS

A. Structural characteristics [$Ba_xCe_{0.85}M_{0.15}O_3$ (*M* = Nd, Gd, Yb; *x* = 0.85–1.20)]

The x-ray powder diffraction patterns of the calcined $Ba_xCe_{0.85}M_{0.15}O_3$ (SSR, $x = 0.85$–1.0, twice calcined) are shown in Fig. 1. For Nd- and Gd-doped samples, single-phase perovskite is obtained when the material is nominally stoichiometric. For Gd-doped samples, very small peaks, due to a fluorite phase with composition $(Ce,Gd)O_{2-\delta}$, are present when $x = 0.95$. For Nd-doped samples, the fluorite phase is present only for highly Ba-deficient samples with $x = 0.85$. In the case of Yb-doped samples, the fluorite phase is observed even in the nominally stoichiometric composition. The phase content determined by x-ray powder diffraction was confirmed by electron microscopy studies. As an example, the backscattered electron images of the $Ba_{0.90}Ce_{0.85}Gd_{0.15}O_{3-\delta}$ and $Ba_{0.95}Ce_{0.85}Gd_{0.15}O_{3-\delta}$samples are shown in Fig. 2. Precipitates of a white fluorite phase of $(Ce,Gd)O_{2-\delta}$ are visible within the gray perovskite matrix.

The cell volume as a function of Ba concentration, *x*, is presented in Fig. 3, for both SSR and MP prepared samples; whereas cell volume as a function of sintering temperature for MP-prepared $BaCe_{0.85}Gd_{0.15}O_{3-\delta}$ is shown in Fig. 4. Over the entire composition range ($x = 0.85$–1.20), Gd-doped samples exhibit the largest cell volume and Yb-doped samples the smallest. Sintered samples (data not shown for clarity) revealed a similar trend. From a simple consideration of ionic radii, one would instead expect the Nd-doped sample to have the greatest cell volume. Moreover, the cell volume of $BaCe_{0.85}Gd_{0.15}O_{3-\delta}$ exhibits a slight but statistically significant and monotonic decrease as a function of increasing sintering temperature, Both of these unexpected results, and the absence of precipitates in the Nd-doped samples, are proposed to be a result of Nd and Gd incorporation onto the Ba^{2+} site, as discussed next.

B. Chemical analysis [$Ba_xCe_{0.85}M_{0.15}O_3$ (*M* = Nd, Gd, Yb; *x* = 0.85-1.20)]

The results of the electron microprobe chemical analysis of sintered $Ba_xCe_{0.85}M_{0.15}O_3$ (*M* = Nd, Gd, Yb;

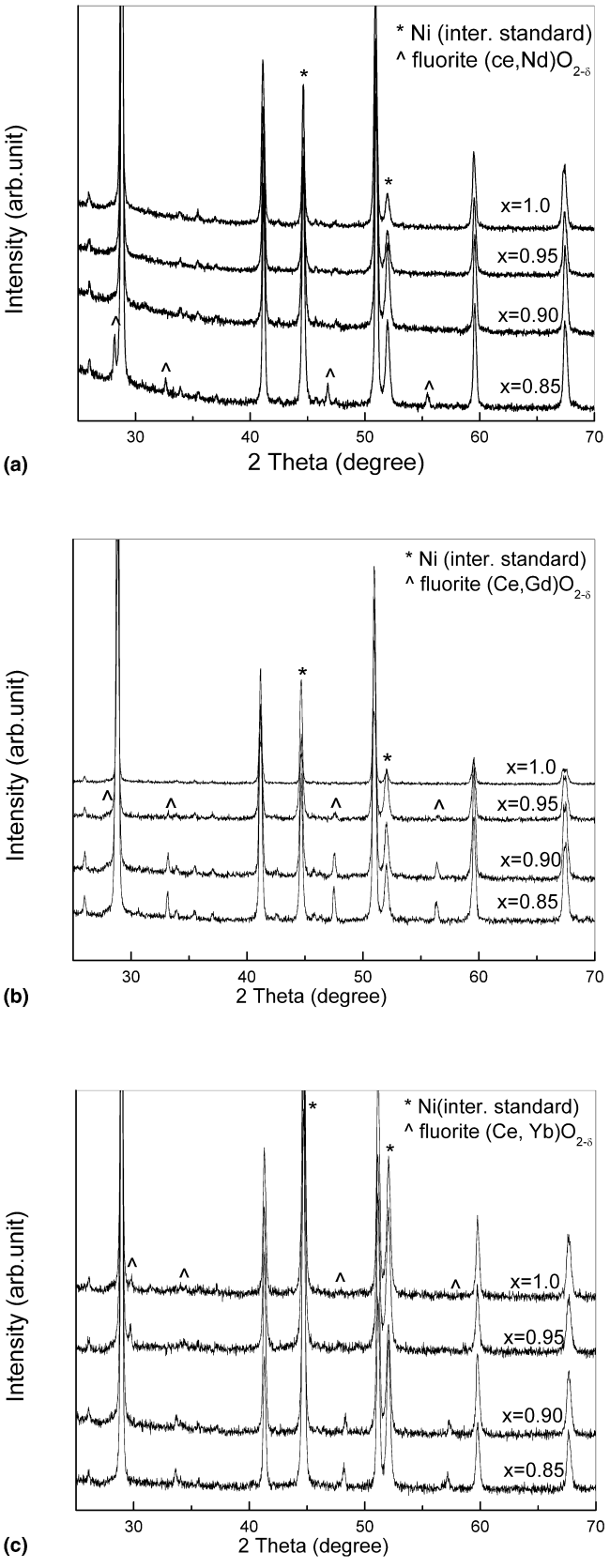

FIG. 1. X-ray diffraction patterns of $Ba_xCe_{0.85}M_{0.15}O_{3-\delta}$ (x = 0.85–1.0) synthesized by solid-state reaction, calcined at 1300 °C/12 h. (a) M = Nd; (b) M = Gd; and (c) M = Yb.

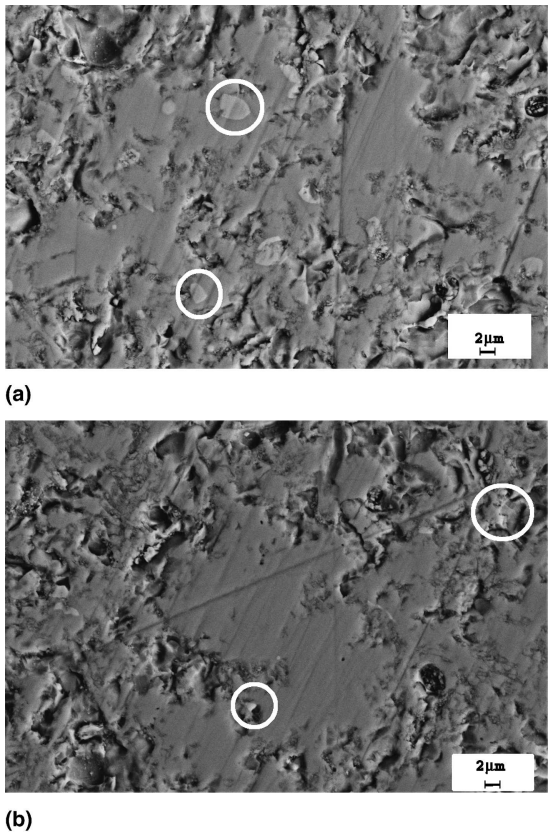

FIG. 2. Backscattered scanning electron microscopy images of sintered (a) $Ba_{0.90}Ce_{0.85}Gd_{0.15}O_{3-\delta}$ and (b) $Ba_{0.95}Ce_{0.85}Gd_{0.15}O_{3-\delta}$ (SSR, sintered at 1550 °C/4 h). Ceria precipitates highlighted.

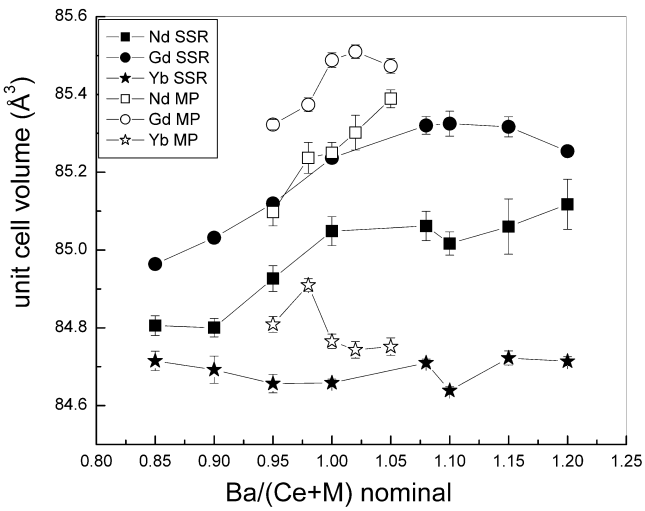

FIG. 3. Dependence of cell volume (per formula unit) of $Ba_xCe_{0.85}M_{0.15}O_{3-\delta}$ (x = 0.85–1.20, M = Nd, Gd, Yb, SSR calcined at 1300 °C/12 h and MP samples calcined at 1300 °C/10 h) on Ba concentration, x.

x = 0.85–1.20) samples are shown in Fig. 5, in which the measured Ba/(Ce+M) ratio is plotted as a function of the nominal value. In some instances a secondary minor phase was present (as noted previously and discussed

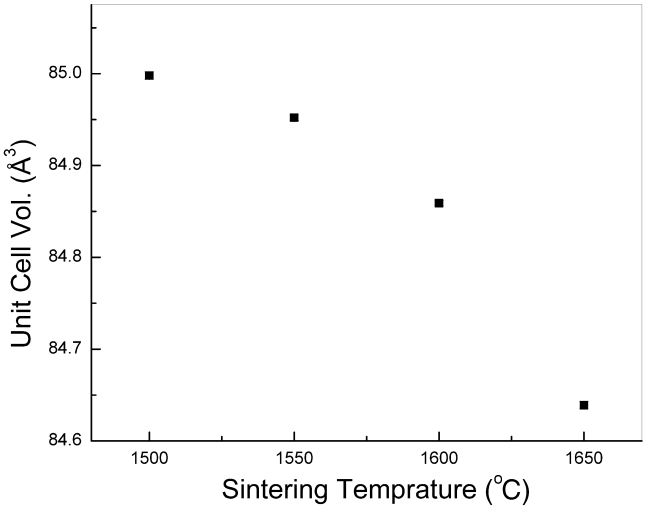

FIG. 4. Dependence of cell volume (per formula unit) of sintered $BaCe_{0.85}Gd_{0.15}O_{3-\delta}$ (MP samples calcined at 1300 °C/10 h) on sintering temperature.

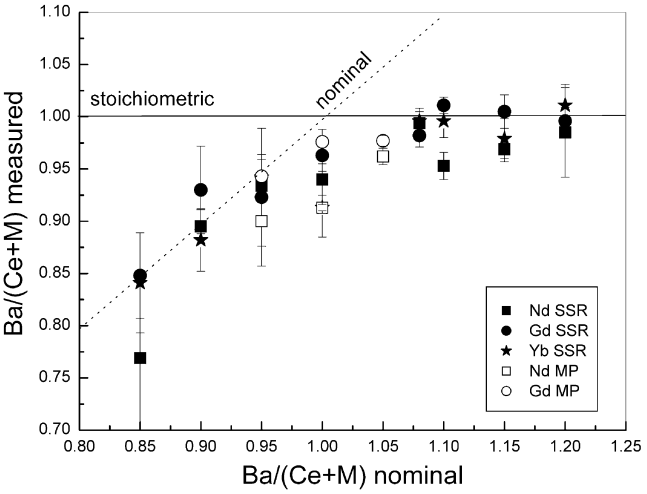

FIG. 5. Chemical composition of sintered $Ba_xCe_{0.85}M_{0.15}O_{3-\delta}$ (M = Nd, Gd, Yb, SSR and MP samples sintered at 1550 °C/4 h), as measured by electron probe microanalysis. In cases where a minor secondary phase was observed, composition reported is that of the major phase.

next in detail); and the compositions shown in Fig. 5 reflect those of the major phase. For almost all of the samples, the experimental molar ratio of Ba/(Ce+M) falls below the nominal value. This tendency is especially pronounced for the nominally barium-rich compositions. For example, a nominal stoichiometry of 20% Ba excess ($Ba_{1.2}Ce_{0.85}Nd_{0.15}O_{3+\delta}$) yields a measured value of at most 3.1% Ba excess, even after accounting for statistical errors in the composition measurement.

Loss of Ba from the bulk region of $Ba_xCe_{0.85}M_{0.15}O_3$ can presumably occur either by barium accumulation in the grain-boundary regions as an amorphous phase, undetectable via conventional x-ray powder diffraction; or by evaporation of BaO at high temperature. A comparison of the EDS spectra from grain boundary and bulk regions of $Ba_{1.2}Ce_{0.85}Nd_{0.15}O_{3+\delta}$ is presented in Fig. 6. Even in the absence of a methodology for quantifying these data, it is evident from the ratios of the characteristic peak intensities that the grain-boundary region contains a much higher molar ratio of Ba/Ce than does the bulk. Thus, it appears that compositions with substantial barium excess can accommodate high Ba concentrations in their grain-boundary regions.

Examination of the cross-section of a sintered (1550 °C/4 h), nominally stoichiometric sample, $BaCe_{0.85}Gd_{0.15}O_{3-\delta}$, confirmed that loss of BaO via evaporation occurs (in addition to possible BaO segregation). The backscattered electron image of this sample (SEM) is shown in Fig. 7, and the corresponding chemical analysis results (electron microprobe) are presented in Fig. 8. A porous, $(Ce,Gd)O_{2-\delta}$ rich layer, around 20-μm in thickness, is evident on the upper surface of the pellet. In contrast, the bulk is dense and chemically homogeneous. The relative content of barium increases with increasing distance from the exterior surface, becoming equal to that of the bulk at approx. 100μm, a distance greater than the thickness of the ceria layer. These sets of experiments indicate that BaO deficiencies are accommodated by a combination of BaO accumulation in the grain-boundary regions and BaO evaporation.

C. H_2O incorporation [$BaCe_{0.85}M_{0.15}O_3$ (M = Nd, Gd, Yb; SSR)]

The results of the thermal gravimetric analysis of H_2O-saturated $BaCe_{0.85}Yb_{0.15}O_{3-\delta}$ are presented in Fig. 9 along with the H_2O signal detected by mass spectroscopy. These data are representative of the three stoichiometric samples examined. Weight loss occurred in two

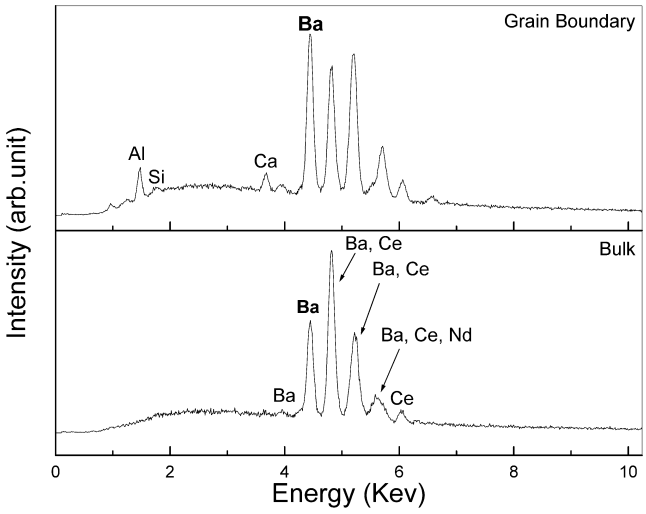

FIG. 6. EDS spectra obtained from the grain-boundary (upper) and bulk (lower) regions of sintered, etched $Ba_{1.2}Ce_{0.85}Nd_{0.15}O_{3+\delta}$ (SSR, sintered at 1550 °C/4 h, etched with concentrated HF).

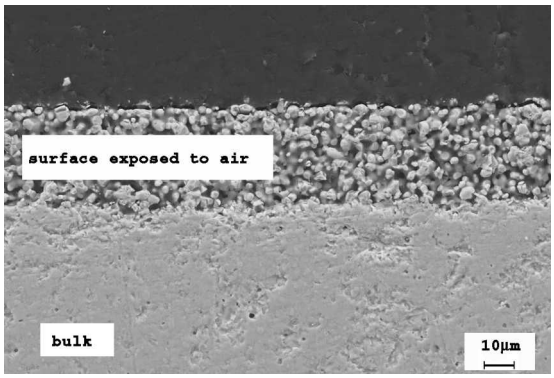

FIG. 7. Backscattered scanning electron microscopy image of the cross-section of sintered $BaCe_{0.85}Gd_{0.15}O_{3-\delta}$ (SSR, sintered at 1550 °C/4 h).

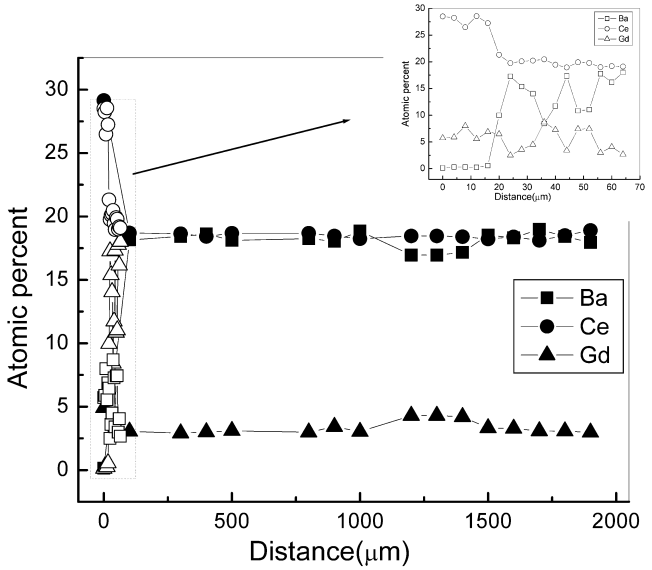

FIG. 8. Chemical composition as a function of distance from the surface, obtained from a cross-section of sintered $BaCe_{0.85}Gd_{0.15}O_{3-\delta}$ (SSR, sintered at 1550 °C/4 h); data collected by WDS (microprobe) methods.

steps, with the first one being completed by 200 °C and the second initiating around 330 °C and peaking at 650 °C. No CO or CO_2 were detected by mass spectroscopy; however, H_2O evolution coincided with these peaks. Accordingly, both weight-loss events are taken to be entirely due to water. The first peak is assigned to the evaporation of surface adsorbed (primarily physisorbed) water, and the second to the loss of water from the bulk of the perovskite material[22] (chemisorbed water). In principle, water uptake in M^{3+}-doped $BaCeO_3$, according to reactions (1) and (2), is independent of the dopant species. It was observed here, however, that the bulk-water content increased in the sequence Nd, Gd, Yb. As discussed next, this trend is believed to result from dopant partitioning over the two cation sites of the perovskite structure.

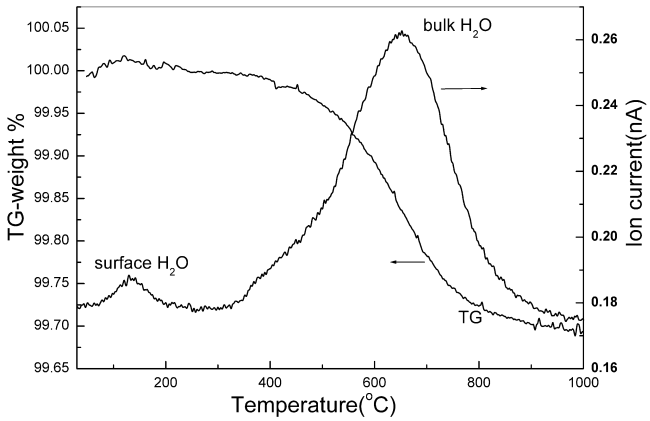

FIG. 9. TGA and mass spectroscopy curves for $BaCe_{0.85}Yb_{0.15}O_{3-\delta}$ obtained under dry argon at 20 °C/min after saturation in an H_2O-containing atmosphere at 500 °C for 20 h.

D. Transport properties [$BaCe_{0.85}M_{0.15}O_3$ (M = Nd, Gd, Yb; SSR)]

The impedance spectra of all samples exhibited well-resolved arcs in the Nyquist representation that could be attributed to bulk (high frequency) and grain-boundary (lower frequencies) response, as well as a quasi-linear portion at the lowest frequencies, corresponding to the electrode response.[23] The bulk conductivity was obtained in the usual manner by correcting for the overall sample geometric factor, A/L, where A is the sample surface area and L the thickness. The temperature dependence of the bulk conductivity of $BaCe_{0.85}M_{0.15}O_{3-\delta}$($M$ = Nd, Gd, Yb) in flowing water-saturated Ar is shown in Fig. 10, in which the data are plotted in Arrhenius form

$$\sigma = \frac{A}{T} e^{-\frac{E_a}{kT}} \quad , \tag{3}$$

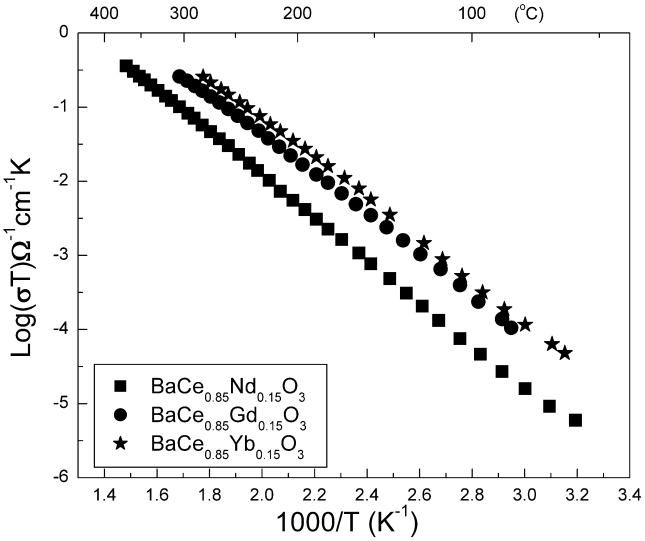

FIG. 10. Conductivity of $BaCe_{0.85}M_{0.15}O_{3-\delta}$ (M = Nd, Gd, Yb, SSR) under flowing, H_2O-saturated Ar.

where σ is the conductivity, A is a pre-exponential term, T is the absolute measurement temperature, k is Boltzman constant and E_a is the activation energy. The results are summarized in Table I. It is evident that the Yb-doped sample exhibits the highest conductivity in wet Ar and the Nd-doped sample the lowest. The activation energy E_a is found to fall between 0.5 eV to 0.6 eV for all three samples, typical for proton conducting oxides[6] and suggestive of similar proton-transport mechanisms.

TABLE I. Electrical properties of nominally stoichiometric $BaCe_{0.85}M_{0.15}O_{3-\delta}$ (SSR samples).

Dopant (M)	Temp. range (°C)	E_a (eV)	A ($\Omega^{-1}cm^{-1}K$)
Nd	80–300	0.57	8469.29
Gd	80–300	0.53	12334.52
Yb	80–400	0.54	27126.95

TABLE II. Ionic radii[24] of relevant elements involved in this study.

	R, Å coordination number 12	R, Å coordination number 6
Ba^{2+}	1.61	
O^{2-}		1.40
Ce^{4+}		0.87
Nd^{3+}	1.27	0.983
Gd^{3+}		0.938
Yb^{3+}		0.868

IV. DISCUSSION

There are several experimental observations presented here that warrant further discussion: the largest cell volumes have been obtained for Gd-doped samples despite the larger ionic radius of the Nd dopant ion; there is an increasing tendency for fluorite precipitation in the sequence Nd < Gd < Yb; and, water uptake and conductivity increase in the same sequence. All of these results, as outlined next, are consistent with a model in which the larger Nd dopant has the greatest tendency to at least partially reside on the Ba site, and the smaller Yb dopant has the least tendency to do so.

A. Cell volume

If one assumes that the trivalent dopant ion is incorporated onto the cerium site, $BaCe_{0.85}M_{0.15}O_{3-\pi\delta}$, the perovskite cell volume should be a monotonic function of dopant ionic radius, as listed in Table II.[24] If, however, as proposed here, Nd is partly incorporated onto the Ba site, then the substitution of the large Ba ion by the smaller Nd ion would be anticipated to yield a cell volume that is smaller than otherwise expected. In comparison to Gd and Yb, the large size of Nd makes it the most amenable to incorporation onto the A site and thus the effect will be greatest for this element.

Ideally, one would like to quantify the relationship between stoichiometry and lattice parameters, and to use this relationship to directly determine the concentration of M cations on the A- and B-sites from the experimental values of the lattice parameters. However, the lattice parameters of a perovskite compound cannot be determined a priori from the ionic radii of the species involved because of the octahedral tilting that is well-known to occur in this structure type. Despite this phenomenon, compilation of the available structural data for known $Ba^{2+}M^{4+}O_3$ perovskites (Table III) reveals that there is an almost ideally linear relationship between the volume per formula unit and the sum of the volumes of the species comprising the formula unit, Fig. 11. The result indicates that the unusual cell-volume behavior observed here for doped barium cerate cannot be readily explained by distortions of the unit cell (as a consequence of octahedral tilting), but it is instead connected to the chemical contents of the unit cell. The correlation implied by the data in Fig. 11 is

$$V_{cell} = -478(44) + 10.3(8) \times V_{sum}\ \text{Å}^3 \quad . \qquad (4)$$

Although the constant term in Eq. (4) has a large negative value, under no conditions is the cell volume less than the sum of the ionic volumes of the species involved. The absolute numerical value of the error due to the fitting process is not small. However, the variation in cell volume between the various samples examined here and the overall deviation from the volume of undoped $BaCeO_3$ are small, and the error within this small range is thus considered negligible.

With this relationship, we can, ideally, use the measured cell volumes to determine the total volume of the species residing on the three sites of the perovskite cell. We first note, however, that this straight line correlation does not pass exactly through the data point for $BaCeO_3$, Fig. 11. Specifically, the experimental cell volume (per formula unit) is 85.550 Å^3, whereas it calculated at

TABLE III. Calculated and experimental unit cell volume of $Ba^{2+}M^{4+}O_{3-\delta}$ perovskite (pseudo cubic structure).

Comp.	$Vol_B{}^{4+}$ (Å^3)	t factor[a]	Vol_{A+B+3O} (Å^3)	V_{ICSD}/unit (Å^3)	Ref. (ICSD#)[b]
$BaTiO_3$	0.9276	1.0615	52.891	64.400	73646
$BaZrO_3$	1.563	1.0040	53.526	74.019	43136
$BaTbO_3$	1.839	0.9854	53.802	78.243	89028
$BaAmO_3$	2.572	0.9460	54.535	82.313	61317
$BaPuO_3$	2.664	0.9418	54.627	84.192	65033
$BaPrO_3$	2.572	0.9460	54.535	83.750	2753
$BaCeO_3$	2.758	0.9376	54.721	85.550	79625
$BaUO_3$	2.953	0.9294	54.916	86.040	84821

[a]t factor $= (r_A + r_o)/\sqrt{2}\,(r_B + r_o)$.

[b]Data are taken from the Inorganic Crystal Structure Database, with the structural reference number as provided in the table.

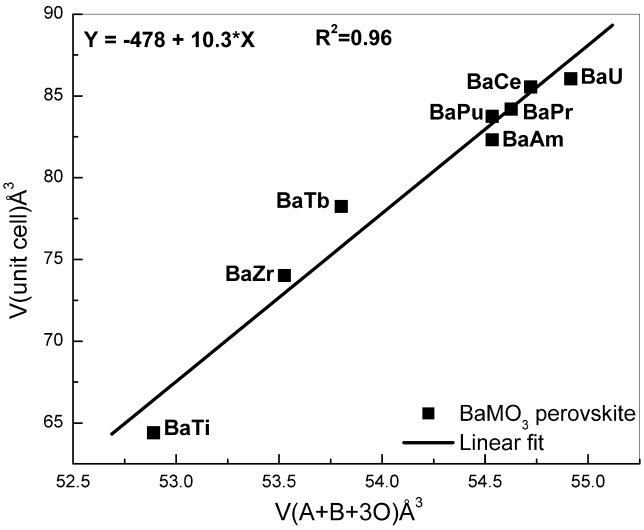

FIG. 11. Psuedo-cubic cell volume of barium-based perovskites as a function of the sum of the ionic radii of the constituent species.

85.240 $Å^3$ from Eq. (4). Accordingly, the relationship is modified by a correction factor to yield the form

$$V_{cell} = -479(44) + 10.3(8) \times V_{sum}\ Å^3 \quad . \qquad (5)$$

To apply this correlation to doped, possibly barium-deficient barium cerate (and to determine the values of three unknowns, A-site occupancy, B-site occupancy, and anion site occupancy, from a single input parameter), we make the following assumptions/approximations: (i) Both A- and B-sites are fully occupied (no cation vacancies). (ii) M-atom occupancy on the barium site will be sufficiently small so as to retain the validity of the correlation curve (derived only for barium-based perovskites) to the new composition. (iii) Anion vacancies, which result to maintain overall charge balance, have the same volume as the oxygen ions that would normally occupy those sites. The first approximation is justified by the experimental observation that even slightly Ba-deficient (undoped) barium cerate is unstable with respect to ceria precipitation,[11] indicating that the concentration of A-site vacancies is extremely small, and from the large coulombic energy penalty expected from the absence of a tetravalent (B-site) ion from its normal site. The third approximation is considered reasonable in light of the volume assigned to an oxygen vacancy in perovskite structure ($R_{Vo}^{\bullet\bullet}$ = 1.4045Å) by Mogensen et al.[25] Combined, these approximations imply that the occupation on the A and B sites can be respectively described as

$$A = \left(\frac{1-2y}{1-y}\right)Ba + \left(\frac{y}{1-y}\right)M \quad , \qquad (6)$$

$$B = \left(\frac{0.85}{1-y}\right)Ce + \left(\frac{0.15-y}{1-y}\right)M \quad , \qquad (7)$$

where $2y/(1-y)$ represents the fraction of Ba lost from the perovskite composition, and $y/(1-y)$ represents the dopant occupancy on the A-site. The parameter y is the amount of dopant on the A-site before normalization for the adjusted stoichiometry of the perovskite.

The volumes associated with these species can then be estimated using the correlation relationship, Eq. (5), and defining the equivalent radii of the A- and B-site cations as the weighted sums of the radii of the species that reside on those sites (taking due care to use the ionic radii appropriate for the 12-fold and 6-fold coordinates at these sites, respectively). Relevant ionic radii are summarized in Table II. This analysis is applied to nominally stoichiometric samples, prepared by both SSR and MP methods. The results, Table IV, presented for both calcined and sintered materials, provide a measure of the extent to which the dopant incorporates on the A-site in nominally stoichiometric compositions. The small cell volume of the Nd-doped sample is now entirely reasonable, and it indicates occupation of the A-site by Nd at about the 2.5% level.

The decrease in cell volume with increasing sintering temperature, Fig. 4, can now be explained in terms of the defect chemistry of doped barium cerate. Upon exposure to high temperatures, BaO evaporates, as evidenced by the presence of a ceria-rich surface layer, Fig. 7. Loss of BaO from the sample interior results in a slightly Ba-deficient sample that readily incorporates Gd onto the A-site, and consequently it has a smaller cell volume than the stoichiometric compound. Using the formalism developed above for relating cell volume to stoichiometry, we estimate the values of Ba/(Ce+Gd) for the samples sintered at 1500 and 1650 °C (the lowest and highest

TABLE IV. Defect chemical parameters of nominally stoichiometric $BaCe_{0.85}M_{0.15}O_{3-\delta}$ as derived from cell volume analysis and microprobe analysis. Number in parenthesis indicates uncertainty in the final digit(s).

Dopant	Nd	Gd	Yb
SSR V(exp.) $Å^3$ 1300 °C/12 h	85.05(4)	85.24(1)	84.66(1)
[M] on A-site	0.023(1)	0.013(0)	0.008(0)
[M] on B-site	0.130(1)	0.139(0)	0.143(0)
δ	0.053(1)	0.063(0)	0.068(0)
Ba/(M + Ce)	0.955(2)	0.974(0)	0.984(0)
SSR V(exp.) $Å^3$ 1550 °C/4 h	84.76(4)	85.05(3)	84.48(2)
[M] on A-site	0.026(1)	0.015(1)	0.010(0)
[M] on B-site	0.128(1)	0.137(0)	0.141(0)
δ	0.051(1)	0.061(0)	0.066(0)
Ba/(M + Ce)	0.949(2)	0.970(1)	0.980(0)
Ba/(M + Ce) microprobe	0.940(15)	0.893(15)	0.913(28)
MP V(exp.) $Å^3$ 1300 °C/10 h	85.25(3)	85.49(2)	84.77(2)
[M] on A-site	0.021(0)	0.011(0)	0.007(0)
[M] on B-site	0.132(0)	0.141(0)	0.144(0)
δ	0.055(0)	0.065(0)	0.068(0)
Ba/(M + Ce)	0.959(0)	0.978(0)	0.986(0)
Ba/(M + Ce) microprobe	0.913(3)	0.976(12)	0.996(12)

temperatures used) to be 0.969(5) and 0.963(5), respectively. The difference is too small to be readily resolved by chemical analysis methods, and thus the hypothesis cannot be easily confirmed. Nevertheless, the conclusive demonstration that BaO loss occurs and that BaO deficiency causes a decrease in cell volume in intentionally Ba-deficient materials, strongly support the proposed explanation.

B. Phase relationships and stoichiometry

The diffraction results, Fig. 3, further imply that there is some compositional range, Ba/(Ce+M), over which the perovskite phase exists; and that this range is dependent on the specific dopant. The observation of a composition independent-lattice constant for Yb-doped samples is consistent with a perovskite phase of fixed stoichiometry, and almost no Yb on the A-site. Furthermore, ceria precipitates were observed for the Yb-doped, barium-deficient samples. In contrast, the Gd- and Nd-doped samples show measurable dependence of the cell volumes on stoichiometry, consistent with the presence of a single phase of variable composition. The increase in volume with increasing barium content is furthermore consistent with the increasing concentration of dopant on the B-site. The trends obtained from the two types of samples, solid-state reaction synthesized and modified Pechini-route synthesized, are similar; but the absolute values of the cell volumes are measurably different (Table IV). The different processing routes likely yield samples with different final barium contents. In addition, the slight difference in defect chemical parameters between calcined and sintered samples (Table IV), is likely attributable to the loss of Ba at high processing temperature, as described already. Indeed, an increase in sintering temperature by just 50 °C in processing temperature can result in a cell-volume decrease of as much as approximately $1Å^3$ (Fig. 4).

The previous discussion, along with the microprobe chemical analysis, Fig. 5, shows that even nominally stoichiometric barium cerate (of nominal composition $BaCe_{1-x}M_xO_{3-\delta}$) is deficient in barium and can have the dopant ion present on the A-site. The maximum concentration of trivalent dopant ion that can be incorporated onto the perovskite A-site can be determined from the compositions at which the ceria phase appears as a precipitate, if one again assumes that both A- and B-sites in the perovskite are fully occupied. Because of significant diffraction peak overlap between the perovskite and fluorite phases, the electron back-scattered images, Fig. 2, and analogous electron microprobe images (not shown) provide greater sensitivity to the presence of ceria precipitates than the x-ray powder diffraction measurements. The compositions, x^*, at which ceria was first observed are summarized in Table V, where x is defined as the compositional ratio, [Ba]/([Ce] + [M]). Samples with x less than or equal to this critical value contained detectable amounts of ceria. Using Eqs. (6) and (7), we note that x is simply $1\text{-}2y$, and the maximum dopant concentration on the A-site, $y/(1\text{-}y)$, is also given as $y/(x + y)$. The maximum values of y and $y/(x + y)$ (which correspond to the maximum amount of dopant on the A-site before and after normalization, respectively) determined from this analysis are also provided in Table V.

Table V. Defect chemistry of doped barium cerate as determined by electron microprobe chemical analysis.

Dopant	x* (a)	Max. y	y/(x + y)	Perovskite composition
Nd (SSR)	0.85	0.075	8.1%	$(Ba_{0.919}Nd_{0.081})(Ce_{0.919}Nd_{0.081})O_3$
Gd (SSR)	0.95	0.025	2.6%	$(Ba_{0.974}Gd_{0.026})(Ce_{0.872}Gd_{0.128})O_{2.49}$
Yb (SSR)	1.0	0	0	$Ba(Ce_{0.85}Yb_{0.15})O_{2.925}$
Nd (MP)	<0.85	>0.75	>8.1%	···
Gd (MP)	0.95	0.025	2.6%	$(Ba_{0.974}Gd_{0.026})(Ce_{0.872}Gd_{0.128})O_{2.949}$
Yb (MP)	0.98	0.01	1.0%	$(Ba_{0.990}Yb_{0.010})(Ce_{0.859}Yb_{0.141})O_{2.935}$

The data reveal that little, if any Yb can be incorporated onto the perovskite A-site, whereas as much as 50% of the Nd dopant can do so. The result obtained here for the Nd doped sample is in excellent agreement with that reported by Makovec et al. in their phase equilibria study of $BaCeO_3$-Nd_2O_3.[9] The existence of the fluorite phase in the nominally stoichiometric Yb-doped sample (SSR) is consistent with the highly B-site specific manner in which this dopant is incorporated into barium cerate. Even slight barium oxide loss from this compound upon high temperature processing cannot be accommodated by dopant partitioning. The small but measurable differences between samples prepared by different routes emphasize the sensitivity of defect chemistry to processing.

C. Oxygen-vacancy concentration, water update and proton conductivity

For an $ABO_{3-\delta}$, perovskite with A- and B-site cations defined by Eqs. (6) and (7), respectively, the oxygen non-stoichiometry, δ, (equivalent to the oxygen vacancy concentration) is given by

$$\delta = \frac{0.075 - y}{1 - y} \quad . \tag{8}$$

In contrast, for doped barium cerate in which all of the trivalent dopant species reside on the B-site, the vacancy concentration is simply $[V_o^{\bullet\bullet}] = 0.075$ for a 15% dopant concentration. Thus, because dopant partitioning reduces the concentration of oxygen vacancies, it can be anticipated to result in water uptake that is lower than in the ideal case. Here, we define the ideal case as one in which, after humidification, all oxygen vacancies are occupied by hydroxyl groups (although such a limit may not be thermodynamically favorable). The experimentally determined water contents in doped, nominally stoichiometric barium cerate, as derived from the TGA measurements of SSR samples, are listed in Table VI. These

TABLE VI. H_2O content relative to various models as measured by thermal gravimetric analysis in nominally stoichiometric $BaCe_{0.85}M_{0.15}O_{3-\delta}$ (SSR samples).

Dopant (M)	δm% (TGA)	$*\delta m_0$% (theo.)	$*\delta m_1$%	$*\delta m_2$%
Nd	0.16	0.42	0.28	0.26(8)
Gd	0.28	0.41	0.34	0.13(17)
Yb	0.31	0.40	0.36	0.18(15)

$*\delta m_0$% (theo.) is the expected weight loss assuming dopants are entirely incorporated onto the B-site and all oxygen vacancies become filled with hydroxyl groups; δm_1% is the expected weight loss assuming the defect chemistry inferred from the cell volume analysis of the sintered samples and further assuming that all oxygen vacancies become filled with hydroxyl groups; δm_2% the expected weight loss assuming the defect chemistry inferred from the electron probe chemical and analysis and further assuming that all oxygen vacancies become filled with hydroxyl groups.

values are compared to: first, what one would expect from a defect chemical model in which only B-site doping occurs, Eq. (1), and all oxygen vacancies are filled with hydroxyl groups upon hydration, Eq. (2). Second, what one would expect from the perovskite composition derived from the cell-volume analysis, as given in Table IV. Third, what one would expect from the experimentally measured perovskite composition, as also given in Table IV.

In all cases, Table VI, water uptake is significantly lower than the ideal. The discrepancy between the ideal and actual values increases with increasing dopant ion size, in agreement with the proposed dopant incorporation model. A difference in proton concentration in the hydrated samples would be expected to manifest itself as a difference in proton conductivities. Specifically, the pre-exponential term of Eq. (3) should be proportional to the concentration of charge carriers. Indeed, the conductivity of Yb-doped barium cerate is the greatest of the three compositions examined; and that of Nd-doped the lowest. Furthermore, the activation energies are generally comparable (although that of Nd is slightly higher than those of Gd and Yb), and the pre-exponential terms vary in a manner similar to the water contents. It appears then that the high conductivity of Yb-doped barium cerium is at least in part due to its optimal defect chemistry, although other factors such as lattice strain upon doping and defect association are likely to also contribute to differences in conductivities for different dopant species.

V. CONCLUSIONS

The defect chemistry, and, in particular, the dopant site incorporation preference in the perovskite $Ba_xCe_{0.85}M_{0.15}O_3$ (M = Nd, Gd, Yb) has been investigated. Within the entire Ba concentration range (x = 0.85–1.20), every sample examined exhibits Ba deficiency relative to the nominal composition. Chemical analysis clearly shows that BaO evaporates from the surface of sintered pellets, and analysis also indicates the possible existence of an amorphous Ba-rich phase at grain boundaries. Barium-oxide deficiency results in a clear decrease in cell volume for Gd and Nd doped samples, in which the trivalent ion can reside on the Ba-site. Cell volume also decreases with increasing sintering temperature, which has been explained in terms of increasing barium deficiency. The inversion of the cell volumes between the Gd-doped and Nd-doped samples results from the more extensive incorporation of Nd^{3+} ions onto the Ba^{2+}-site. As a consequence of the greater ability of larger cations to exist on the Ba-site, the H_2O adsorption and proton conductivities of large-cation doped barium cerates are lower than those of small-cation doped analogs. Microprobe analysis, water incorporation measurements, and the impedance spectroscopy support these conclusions and yield a semi-quantitative measure of the concentration of dopant species on the A-site. The compositional limits for the maximum Ba^{2+}-site incorporation, as determined experimentally for the three dopant ions examined, are given as: $(Ba_{0.919}Nd_{0.081})(Ce_{0.919}Nd_{0.081})O_3$, $(Ba_{0.974}Gd_{0.026})(Ce_{0.872}Gd_{0.128})O_{2.875}$, and $Ba(Ce_{0.85}Yb_{0.15})O_{2.925}$.

ACKNOWLEDGMENTS

The authors thank Dr. Chi Ma (California Institute of Technology) for assistance with the scanning electron microscopy and microprobe analysis. Caltech analytical facilities are partially supported by the National Science Foundation through the Caltech Center for the Science and Engineering of Materials. Funding of this work has been provided by the U.S. Department of Energy through the Office for Energy Efficiency and Renewable Energy.

REFERENCES

1. M.A. Pena and J.L.G. Fierro: Chemical structures and performance of perovskite oxides. *Chem. Rev.* **101,** 1981 (2001).
2. K.R. Kendall, C. Navas, J.K. Thomas, and H.C. zurLoye: Recent developments in perovskite-based oxide ion conductors. *Solid State Ionics* **82,** 215 (1995).
3. H. Iwahara, H. Uchida, K. Ono, and K. Ogaki: Proton conduction in sintered oxides based on $BaCeO_3$. *J. Electrochem. Soc.* **135,** 529 (1988).
4. H. Uchida, N. Maeda, and H. Iwahara: Relation between proton and hole conduction in $SrCeO_3$-based solid electrolytes under water-containing atmospheres at high-temperatures. *Solid State Ionics* **11,** 117 (1983).
5. T. Yajima, H. Suzuki, T. Yogo, and H. Iwahara: Protonic conduction in $SrZrO_3$-based oxides. *Solid State Ionics* **51,** 101 (1992).
6. K.D. Kreuer: Proton-conducting oxides. *Annu. Rev. Mater. Res.* **33,** 333 (2003).
7. H. Iwahara, H. Uchida, and K. Morimoto: High temperature solid electrolyte fuel cells using perovskite-type oxide based on $BaCeO_3$. *J. Electrochem. Soc.* **137,** 462 (1990).

8. H. Iwahara, H. Uchida, K. Ogaki, and H. Nagato: Nernstian hydrogen sensor using $BaCeO_3$-based, proton-conducting ceramics operative at 200°C–900°C. *J. Electrochem. Soc.* **138,** 295 (1991).
9. D. Makovec, Z. Samardžija, and D. Kolar: Solid solubility of neodymium in $BaCeO_3$. *J. Am. Ceram. Soc.* **80,** 3145 (1997).
10. Y. Tsur, A. Hitomi, I. Scrymgeour, and C.A. Randall: Site occupancy of rare-earth cations in $BaTiO_3$. *Jpn. J. Appl. Phys.* **40,** 255 (2001).
11. D. Shima and S.M. Haile: The influence of cation nonstoichiometry on the properties of undoped and gadolinia-doped barium cerate. *Solid State Ionics* **97,** 443 (1997).
12. A. Yamada and Y.M. Chiang: Nature of cation vacancies formed to compensate donors during oxidation of barium-titanate. *J. Am. Ceram. Soc.* **78,** 909 (1995).
13. E. Brzozowski and M.S. Castro: Defect profile and electrical properties of Nb_2O_5-doped $BaTiO_3$ materials. *J. Mater. Sci. Mater. Electron.* **14,** 471 (2003).
14. G. Ma, T. Shimura, and H. Iwahara: Simultaneous doping with La^{3+} and Y^{3+} for Ba^{2+} and Ce^{4+}-sites in $BaCeO_3$ and ionic conduction. *Solid State Ionics* **120,** 51 (1999).
15. M.T. Buscaglia, V. Buscaglia, and M. Viviani: Atomistic simulation of dopant incorporation in barium titanate. *J. Am. Ceram. Soc.* **84,** 376 (2001).
16. R.A. Davies, M.S. Islam, and J.D. Gale: Dopant and proton incorporation in perovskite-type zirconates. *Solid State Ionics* **126,** 323 (1999).
17. V. Agarwal and M. Liu: Preparation of barium cerate-based thin films using a modified Pechini process. *J. Mater. Sci.* **32,** 619 (1997).
18. I.U.C.R. Powder Diffraction: 22, **21** (1997)
19. K.S. Knight and N. Bonanos: Space group and lattice constants for barium cerate and minor corrections to the crystal structures of $BaCe_{0.9}Y_{0.1}O_{2.95}$ and $BaCe_{0.9}Gd_{0.1}O_{2.95}$. *J. Mater. Chem.* **4,** 899 (1994).
20. J.T. Armstrong: CITZAF - A package of correction programs for the quantitative electron microbeam x-ray-analysis of thick polished materials, thin-films, and particles. *Microbeam Anal.* **4,** 177 (1995).
21. B.B. Boukamp: Equivalent Circuit, University of Twente, The Netherlands (1988).
22. A. Kruth and J.T.S. Irvine: Water incorporation studies on doped barium cerate perovskite. *Solid State Ionics* **162–163,** 83 (2003).
23. S.M. Haile, D.L. West, and J. Campbell: The role of microstructure and processing on the proton conducting properties of gadolinium-doped barium cerate. *J. Mater. Res.* **13,** 1576 (1998).
24. R.D. Shannon: Revised effective ionic radii and systematic studies of interatomic distances in halides and chalcogenides. *Acta Crysta. A* **32,** 751 (1976).
25. M. Mogensen, D. Lybye, N. Bonanos, P.V. Hendriksen, and F.W. Poulsen: The Effect of Lattice Stress In Ion Conducting Fluorites And Perovskites. *Electrochemical Society Proceedings.* 2001 **28,** 15 (2002).